ACS OMEGA

http://pubs.acs.org/journal/acsodf

Article

Effect of Fe(III) Modification on the Phosphorus Removal Behavior of Ce(III) Carbonate Adsorbents

Jie Yang, Zuobei Wang, Ruonan Li, Xiaofeng Xu, Junrui Liu, You-Gui Huang, Xin Ye,* and Wei Wang*

Cite This: *ACS Omega* 2022, 7, 31767−31777

Read Online

ACCESS | Metrics & More | Article Recommendations | Supporting Information

ABSTRACT: Excessive phosphorus (P) in water is the main reason for eutrophication, which has been a global problem for many years. For the adsorption treatment of phosphorus-containing wastewater, adsorbents are key research topics. In this study, we develop the synthesis of a series of Ce/Fe adsorbents by modifying the commercial cerium carbonate with $Fe_2(SO_4)_3$. By conducting comprehensive analysis with XRD, FTIR, and SEM, we find that the amorphous granular structure and large chunky structure created by the high and low Fe content, respectively, both had a negative effect on the adsorption capacity of phosphate. Among different adsorbents, Ce/Fe-15/3, with Ce loading of 28.33 wt % and Fe loading of 5.66 wt %, exhibits high P adsorption capacity of 58 mg P/g (in pH = 7, 30 mg P/L solution). It also demonstrates excellent selectivity toward phosphate adsorption in Cl^-, SO_4^{2-}, and NO_3^- solution (up to 20 times of the phosphate molarity) and good adsorption stability in acidic environments (pH = 3−6). The adsorption behavior of Ce/Fe-15/3 can be modeled well by the Langmuir model and pseudo-second-order (PSO) model. By conducting the XPS analysis, we conclude that the adsorption mechanism is a combination effect of Ce/PO_4^{3-} and Fe/PO_4^{3-} chemical interactions.

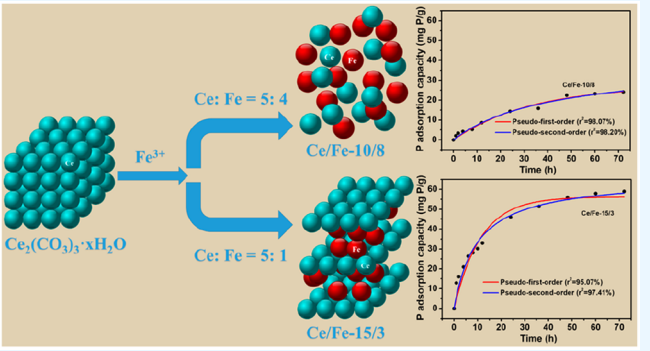

1. INTRODUCTION

Nowadays, the worldwide eutrophication phenomenon has attracted significant attention around the world.[1] The excessive nutrients in the water body make algae bloom wildly, resulting in the death of other aquatic organisms.[2] Among different reasons leading to the eutrophication, excessive phosphorus (P) is a main factor. Phosphorus in water comes from a wide range of sources, including agricultural wastewater, industrial wastewater, and urban domestic sewage.[3] Orthophosphate is the main form of phosphorus in these sources. It is soluble and can be easily absorbed and utilized by algae. Therefore, effective treatments on the orthophosphate pollutants are critical for solving the eutrophication problem caused by the excessive phosphorus content.[4] Among different treatment methods (e.g., chemical precipitation methods and biological methods), the adsorption treatment is widely used because of its large capacity, fast kinetics, low energy consumption, and possible recyclability.[5] New adsorbents with high adsorption capacity, good selectivity, and a simple preparation procedure need to be developed.[6]

The adsorption of phosphorus on adsorbents is usually achieved via either physical adsorption or chemical adsorption.[7] The adsorption mechanism of different adsorbents varies dramatically.[8] Because of the strong binding effect between rare-earth ions and anionic pollutants,[9] rare-earth-based materials are often used to adsorb anionic pollutants in the environment.[10] Li et al.[11] found that the adsorption of both trivalent arsenic ions and pentavalent arsenic ions by hydrous cerium oxide nanoparticles reaches a high capacity over 100 mg/g, higher than most commercial arsenic removal adsorbents. Na et al.[12] found that the adsorption capacity of lanthanum hydroxide for fluoride ions was as high as 242 mg/g. For adsorbing phosphate ions, it is worth mentioning that rare-earth phosphates exhibit very low K_{sp} values, making rare-earth ions extremely effective in capturing phosphate species. Goscianska et al.[13] loaded La onto the molecular sieves extracted from fly ash and obtained adsorbents exhibiting excellent phosphate removal properties. Lu et al.[14] proved that rare-earth carbonates (e.g., $La_2(CO_3)_3$) are promising adsorbents for phosphorus adsorption.

As a light rare-earth element with abundant reserves,[15] cerium-based materials are widely used as phosphorus removal adsorbents because of their strong chemical interaction with phosphate ions in solution.[16] As a cheap cerium-containing species, cerium carbonate could be a promising adsorbent choice. However, previous research also showed that single-

Received: April 12, 2022
Accepted: July 28, 2022
Published: August 29, 2022

component materials exhibited limitations in performance.[17] As a result, several single-component materials were usually combined to form composite materials for improving the material properties.[18] Taking the cerium-based compounds as examples, Su et al.[19] used different proportions of zirconium to dope cerium oxide and obtained cerium−zirconium binary metal oxides for enhancing the phosphorus adsorption. Wang et al.[20] utilized coprecipitation of iron oxide and ceria to improve the adsorption performance. Compared with cerium oxide,[21] the layered structure of cerium carbonate[22] possesses cerium active sites that are easily accessible for the phosphate adsorption process. Enhancement in the adsorption effect could be achieved by exploiting alternative doping elements.[23]

In this study, commercial $Ce_2(CO_3)_3{\cdot}xH_2O$ with a layered structure is modified by $Fe_2(SO_4)_3$ to prepare a series of Ce/Fe bimetallic adsorbents. The differences in the crystal structure, morphology, and adsorption effects of these samples with different cerium/iron ratios are characterized and discussed. The adsorption mechanism is probed by XRD, FTIR, and XPS to determine the interaction between phosphate ions and the adsorbents.

2. MATERIALS AND METHODS

2.1. Materials. $Ce_2(CO_3)_3{\cdot}xH_2O$, $Fe_2(SO_4)_3{\cdot}xH_2O$, and KH_2PO_4, all of analytical grade, were supplied by Titan Greagent Chemical Co., Ltd. (Shanghai, China). All of the phosphate solutions were prepared by dissolving KH_2PO_4 in deionized (DI) water.

2.2. Synthesis of Phosphate Adsorbents. In the pre-experiment, three samples were synthesized. Volumes of 100 mL of deionized water were measured and added to three beakers. Ferric sulfate was weighed and dissolved in the three beakers to achieve three solutions with the Fe^{3+} concentrations of 0.12, 0.09, and 0.06 mol/L. The three solutions were heated at 60 °C with magnetic stirring at 300 rpm until complete dissolution. Next, three portions of cerium carbonate were weighed according to the Ce^{3+}:Fe^{3+} ratios of 1:2, 1:1, and 2:1, with reference to the Fe^{3+}concentrations of 0.12, 0.09, and 0.06 mol/L, respectively. The cerium carbonate powder was added slowly to the corresponding ferric sulfate solution, resulting in three mixtures with the same metal concentration of 0.18 mol/L. The mixtures were stirred magnetically at 300 rpm at 60 °C for 10 h. The resulted solid products were filtered and washed three times with deionized water. After drying in an oven at 60 °C for 24 h, three samples were obtained, which were named Ce/Fe-6/12 (Ce^{3+}:Fe^{3+} = 1:2), Ce/Fe-9/9 (Ce^{3+}:Fe^{3+} = 1:1), and Ce/Fe-12/6 (Ce^{3+}:Fe^{3+} = 2:1).

For synthesizing the final adsorbents, 100 mL of ferric sulfate solution was made in each of eight beakers with the concentrations of Fe^{3+} being 0.08, 0.07, 0.06, 0.05, 0.04, 0.03, 0.02, and 0.01 mol/L. The solutions were heated at 60 °C with magnetic stirring at 300 rpm until complete dissolution. Cerium carbonate was weighed and added slowly to the eight solutions, resulting in eight mixtures with the corresponding Ce^{3+} to Fe^{3+} ratios of 10:8, 11:7, 12:6, 13:5, 14:4, 15:3, 16:2, and 17:1. The total metal-ion concentration was 0.18 mol/L for all mixtures. The mixtures were stirred magnetically at 300 rpm at 60 °C for 10 h. After that, the solid products were filtered and washed three times with deionized water. Finally, the products were dried at 60 °C for 24 h to obtain eight adsorbents, namely Ce/Fe-10/8, Ce/Fe-11/7, Ce/Fe-12/6, Ce/Fe-13/5, Ce/Fe-14/4, Ce/Fe-15/3, Ce/Fe-16/2, and Ce/Fe-17/1.

2.3. Materials Characterization. Powder X-ray diffraction (XRD) of various samples was characterized on a Miniflex600 (Rigaku, Japan) equipped with Cu K_α radiation (40 kV, 15 mA), and the data were collected in the two-theta range of 5−50° with a scan rate of 5°/min. Scanning electron microscopy (SEM, Apreo S LoVac, Czech) was used for imaging the morphology of the samples, with the acceleration voltage set to 2.0 kV. Fourier transform infrared (FTIR) spectra were recorded on a Nicolet iS 50 FTIR instrument with a DTGS KBr detector, by averaging over 32 scans with a data interval of 0.482 cm^{-1}. Thermogravimetric analysis (TGA) was conducted from room temperature to 800 °C on a TGA/DSC-1 instrument (Mettler Toledo, Switzerland) in an Ar atmosphere with a heating rate of 10 °C/min. The ratio between iron and cerium in the sample was determined by inductively coupled plasma optical emission spectrometry (ICP-OES, Horiba Jobin Yvon, France). X-ray photoelectron spectroscopy (XPS) was performed on an AXIS SUPRA (Kratos, UK) with an Al anode. The XPS data was analyzed by the XPSPEAK41 software.

2.4. Evaluation of the Phosphorus Adsorption Performance of Different Adsorbents. *2.4.1. Static Adsorption Experiment.* For conducting the measurements, a phosphorus-containing stock solution was made. In specific, 1.5 L of KH_2PO_4 solution with the phosphorus concentration of 30 mg/L was prepared, with its pH adjusted to 7 by HCl solution and NaOH solution.

To characterize the static adsorption, 100 mL of phosphorus-containing stock solution was added into a 150 mL conical flask, and 50 mg of the absorbent was added into each conical flask. After that, the conical flask was placed on an incubator shaker at 180 rpm for 48 h at 25 °C. After the adsorption process, about 5 mL of the solution was drawn and filtered through a 0.45 μm membrane filter, for measuring the remaining phosphate concentration and the final pH.

The phosphate concentration was determined by the molybdenum blue spectrophotometric method (GB 11893−89) using a UV/vis spectrometer (UV-1100, Mapada instruments, China). The P adsorption capacity (mg/g) of the adsorbent at equilibrium and at any time t (h) are labeled as q_e and q_t, respectively. They are calculated based on eqs 1 and 2

$$q_e = \frac{(C_0 - C_e)V}{M} \tag{1}$$

$$q_t = \frac{(C_0 - C_t)V}{M} \tag{2}$$

, where C_0, C_e, and C_t are the P concentration (mg/L) in the solution at the beginning, at equilibrium, and at any time t (h), respectively; M is the mass of adsorbent (mg), and V is the volume of the solution (mL).

2.4.2. Selectivity and pH-Stability Measurements. To characterize the selectivity of the adsorbents toward phosphate adsorption, competing anions (including Cl^-, SO_4^{2-}, NO_3^-, HCO_3^-, SiO_3^{2-}, and humic acid (HA)) were introduced as their sodium salts into the phosphorus-containing stock solution (30 mg P/L) without adjusting the initial pH (at about 6.0). This is to avoid the influence of additional ions. The molar ratios between the competing ion and the phosphate ion are set to 1:1, 5:1, 10:1, and 20:1. To a 150 mL flask containing 100 mL of different phosphate solutions, 50 mg of the adsorbent was dispersed and allowed to adsorb

https://doi.org/10.1021/acsomega.2c02269
ACS Omega 2022, 7, 31767−31777

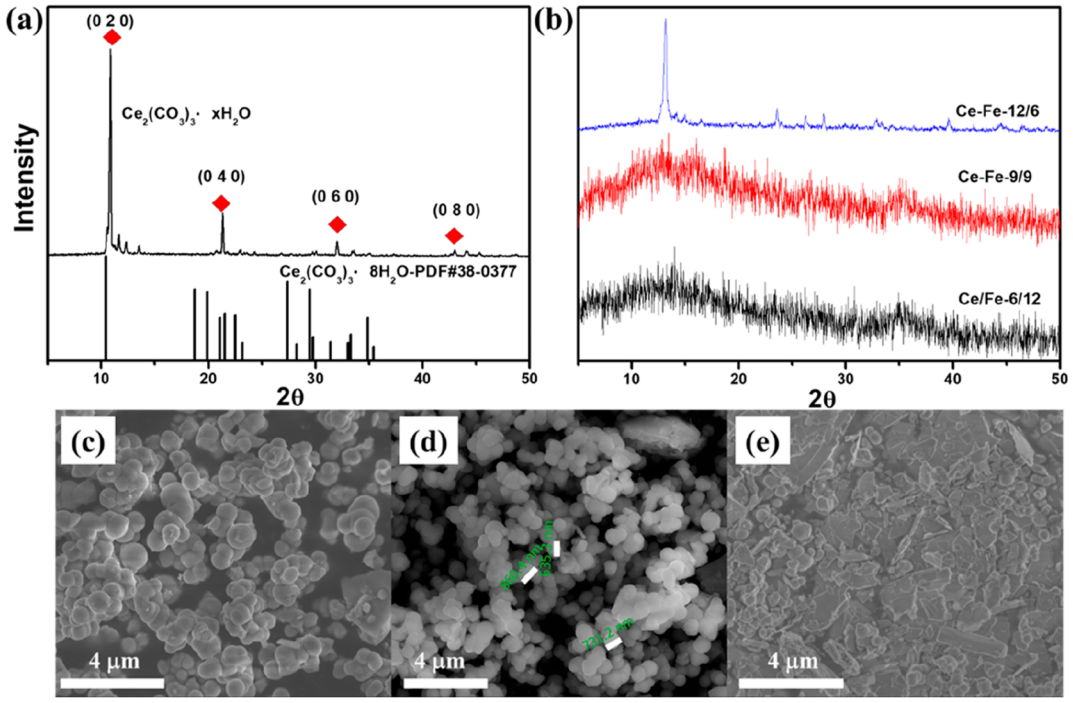

Figure 1. (a) XRD pattern of $Ce_2(CO_3)_3{\cdot}xH_2O$; (b) XRD patterns of Ce/Fe-6/12, Ce/Fe-9/9, and Ce/Fe-12/6; (c–e) SEM images of Ce/Fe-6/12, Ce/Fe-9/9, and Ce/Fe-12/6.

for 48 h before analyzing the remaining P content in the solution.

The pH stability of the adsorbent was characterized to evaluate the phosphate adsorption capacity at different solution pH values. Here, the pH of the phosphate solution (30 mg P/L) was adjusted to 3, 4, 5, 6, 7, 8, 9, 10, and 11 by HCl or NaOH solutions. After the 48 h static adsorption process, the solutions were collected and filtered for analyzing the remaining phosphorus concentration.

2.4.3. Adsorption Kinetic Measurements. Adsorption kinetic measurements were conducted for 72 h in a 1000 mL bottle containing 500 mL of the phosphorus-containing stock solution. The results were fit by the pseudo-first-order (PFO) model, the pseudo-second-order (PSO) model, and the Weber-Morris model (see Supporting Information). The PFO and PSO models are listed as eqs 3 and 4, respectively

$$\frac{dq_t}{dt} = k_1(q_e - q_t) \tag{3}$$

$$\frac{dq_t}{dt} = k_2(q_e - q_t)^2 \tag{4}$$

, where q_e and q_t are the P adsorption capacity (mg/g) of the adsorbent at equilibrium and at any time t (h), respectively; k_1 corresponds to the PFO adsorption rate constant (h^{-1}), and k_2 is the PSO adsorption rate constant (g/(mg·h)).

2.4.4. Adsorption Isotherm Measurements. The adsorption isotherm of the adsorbent was measured in solutions with different phosphorus concentrations (i.e., 5–90 mg P/L). The results were fit by the Langmuir model (eq 5), the Freundlich model (eq 6), and the Temkin model (see Supporting Information), shown as below

$$q_e = \frac{q_m K_L C_e}{1 + K_L C_e} \tag{5}$$

, where q_e is the adsorption capacity at equilibrium (mg/g), q_m is the maximum adsorption capacity in theory (mg/g), C_e is the phosphorus concentration at equilibrium (mg/L), and K_L is the Langmuir constant (L/mg)

$$q_e = K_F C_e^{1/n} \tag{6}$$

, where C_e is the phosphorus concentration at equilibrium (mg/L), K_F is the Freundlich constant (mg/g), and n is an empirical constant.

3. RESULTS AND DISCUSSION

3.1. Materials Characterization of Adsorbents. Properties of single-component materials are often limited,[24] so two or more materials are usually combined to form composite materials for enhancing the material properties.[25] Prior to synthesizing the composite materials, the structure and properties of the single-component material need to be investigated. To determine the composition of pure $Ce_2(CO_3)_3{\cdot}xH_2O$, XRD measurements are performed, and the resulting patterns are shown in Figure 1a. Characteristic diffraction peaks appear at 10.8, 21.3, 32.0, and 43.0°, corresponding to the (0 2 0), (0 4 0), (0 6 0), and (0 8 0) lattice planes, respectively, of $Ce_2(CO_3)_3{\cdot}8H_2O$ (PDF#38–0377). The diffraction pattern indicates that this material possesses a structure with a preferential orientation.[26] Meanwhile, the TGA curve of pure $Ce_2(CO_3)_3{\cdot}xH_2O$ is shown in Figure S1. The weight loss indicates that there are 10 crystalline water molecules in the pure $Ce_2(CO_3)_3{\cdot}xH_2O$.

Next, we perform pre-experiments to see the modification effects by ferric sulfate. The XRD patterns of the three samples are shown in Figure 1b. It is clear that Ce/Fe-6/12 and Ce/Fe-

https://doi.org/10.1021/acsomega.2c02269
ACS Omega 2022, 7, 31767–31777

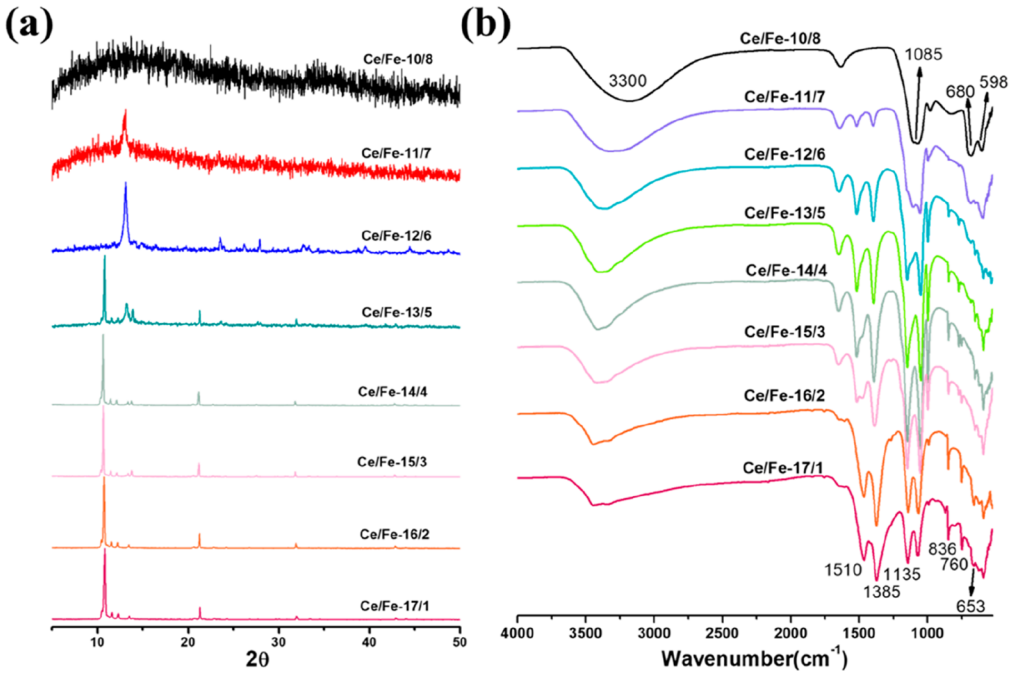

Figure 2. (a) XRD patterns and (b) FTIR spectra of different Ce/Fe adsorbents.

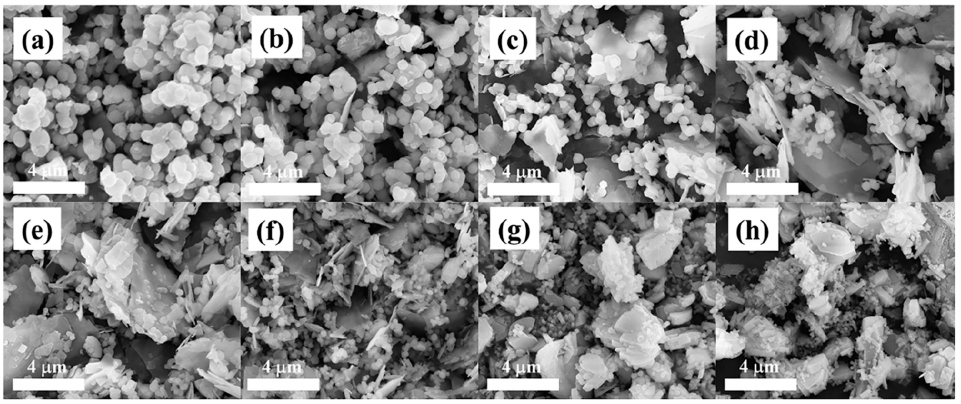

Figure 3. SEM images of (a) Ce/Fe-10/8, (b) Ce/Fe-11/7, (c) Ce/Fe-12/6, (d) Ce/Fe-13/5, (e) Ce/Fe-14/4, (f) Ce/Fe-15/3, (g) Ce/Fe-16/2, and (h) Ce/Fe-17/1.

9/9 are amorphous. In contrast, a characteristic diffraction peak at 13.2° is observed in Ce/Fe-12/6, which might be attributed to the (0 1 0) diffraction of $Ce_2(CO_3)_3{\cdot}4H_2O$ (PDF#06−0076). SEM images of Ce/Fe-6/12, Ce/Fe-9/9, and Ce/Fe-12/6 are shown in Figure 1(c−e). Both Ce/Fe-6/12 and Ce/Fe-9/9 with relatively high Fe content consist of small particles sized between 500 nm and 1 μm. On the other hand, Ce/Fe-12/6 with lower Fe content exhibits a flake morphology with granular particles sandwiched in-between. As a result, we find that the structure and morphology of $Ce_2(CO_3)_3{\cdot}xH_2O$ are greatly altered by the Ce/Fe ratio.

To investigate the modification effects in details, eight adsorbents with different Ce/Fe ratios are produced and characterized. The obtained XRD patterns are shown in Figure 2a. Similar to Ce/Fe-6/12 and Ce/Fe-9/9, Ce/Fe-10/8 is amorphous without any characteristic diffraction peaks. Ce/Fe-11/7 is basically an amorphous structure but with a weak diffraction peak at 13.2°. With the Ce/Fe ratio increasing beyond Ce/Fe-12/6, diffraction signals could be observed. In specific, Ce/Fe-12/6 exhibits an XRD pattern similar to Ce/Fe-12/6, with a characteristic diffraction peak at 13.2°. Since Ce/Fe-12/6 is produced from the same procedure as Ce/Fe-12/6, this indicates the excellent reproducibility of the synthesis. For Ce/Fe-13/5, Ce/Fe-14/4, and Ce/Fe-15/3, the XRD patterns appear similar to the pure $Ce_2(CO_3)_3{\cdot}xH_2O$, with diffraction characteristic peaks at 10.8, 21.3, 32.0, and 43.0°. The diffraction signal at 13.2° can be observed in the XRD patterns of Ce/Fe-13/5, Ce/Fe-14/4, and Ce/Fe-15/3, revealing the coexistence of $Ce_2(CO_3)_3{\cdot}4H_2O$ (PDF#06−0076) in these samples. However, this 13.2° diffraction signal decreases with the increasing Ce content and disappears in the XRD patterns of Ce/Fe-16/2 and Ce/Fe-17/1.

FTIR spectra of these Ce/Fe adsorbents are shown in Figure 2b. In Ce/Fe-10/8 (with the highest Fe content), the broad peak at 3300 cm^{-1} and the characteristic peak at 1085 cm^{-1} are caused by the stretching and bending vibrations, respectively, of the −OH groups in the crystallization water molecules.[27] The characteristic peaks at 598 and 680 cm^{-1} correspond to

https://doi.org/10.1021/acsomega.2c02269
ACS Omega 2022, 7, 31767−31777

the Ce−O and Fe−O stretching vibrations, respectively.[28] With the decreasing Fe content, the vibration signals at 3300, 1085, and 680 cm^{-1} diminish gradually. Meanwhile, the vibrational signals of the CO_3^{2-} groups start to appear: the asymmetric stretching signals of CO_3^{2-} are located at 1510 and 1385 cm^{-1}, the characteristic peaks at 1135 and 760 cm^{-1} represent the symmetrical stretching vibration and symmetrical bending vibration of CO_3^{2-}, respectively, and the peaks at 836 and 653 cm^{-1} are attributed to the asymmetric bending vibrations of CO_3^{2-}.[29] It is worth mentioning that the intensities of these characteristic peaks all become stronger with the decreasing Fe content, confirming the gradually increasing cerium carbonate component. For example, the ICP-OES result shows that the Ce loading (wt %) and Fe loading (wt %) of Ce/Fe-15/3 are 28.33% and 5.66%, respectively.

The SEM images in Figure 3 show an unexpected morphology change of the adsorbents with the varying Fe content. Ce/Fe-10/8 and Ce/Fe-11/7, with the highest iron content, both consist of small particles. In Ce/Fe-12/6, a flake-like structure appears, with a large amount of granular particles mixing in-between flakes. When the iron content keeps decreasing, Ce/Fe-13/5, Ce/Fe-14/4, and Ce/Fe-15/3 all exhibit lamellar structures, with the number of granular particles gradually decreasing. Finally, Ce/Fe-16/2 and Ce/Fe-17/1, with high Ce content, mainly consist of chunks larger than 10 μm with smaller debris scattered in-between. We also conduct elemental mapping on Ce/Fe-15/3 to revolve the distribution of Ce and Fe. The results are shown in Figure S2. Clearly, both Ce and Fe are uniformly distributed on the surface of Ce/Fe-15/3. The signal from Ce appears to be more intensive than that of Fe, which is consistent with the composition of this compound.

3.2. Static Phosphate Adsorption of Adsorbents. First, static adsorption tests are carried out on pure $Ce_2(CO_3)_3{\cdot}xH_2O$ and the three samples produced in the pre-experiment. The results are shown in Table 1. The adsorption capacity of pure $Ce_2(CO_3)_3{\cdot}xH_2O$ is 29.96 mg P/g, which removes about 50% of the phosphorus in the solution. In the three pre-experimental samples, it is clear that the adsorption capacity and effluent pH increase with the increasing cerium content. The adsorption capacity of Ce/Fe-12/6 reaches 57.65 mg P/g, which is larger than the pure $Ce_2(CO_3)_3{\cdot}xH_2O$, proving the beneficial effect of introducing iron modification.

Table 1. Static Adsorption Results of Pure $Ce_2(CO_3)_3{\cdot}xH_2O$ and Three Pre-experiment Samples[a]

	$Ce_2(CO_3)_3{\cdot}xH_2O$	Ce/Fe-6/12	Ce/Fe-9/9	Ce/Fe-12/6
Adsorption capacity (mg P/g)	29.96	10.22	18.25	57.65
Final pH	8.35	4.08	4.14	6.02

[a]25 °C, reaction time = 48 h, C_0 = 30 mg P/L, adsorbent dosage = 0.5 g/L.

For the purpose of obtaining the optimal Ce/Fe ratio, static adsorption experiments were carried out on the eight adsorbents with different Ce/Fe ratios. The results are shown in Figure 4. The adsorption capacity values of Ce/Fe-10/8 and Ce/Fe-11/7 are both below 30 mg P/g, which are lower than the pure $Ce_2(CO_3)_3{\cdot}xH_2O$. With the increasing Ce content, Ce/Fe-12/6, Ce/Fe-13/5, Ce/Fe-14/4, and Ce/Fe-15/3 all exhibit adsorption capacities near 58 mg P/g, removing almost all of the phosphorus from the solution. However, when the Ce content keeps increasing, the adsorption capacities of Ce/Fe-16/2 and Ce/Fe-17/1 decrease. It appears that having cerium carbonate as the major component is critical for achieving high adsorption capacity, while maintaining the iron content at a proper level (i.e., in the range defined by Ce/Fe-12/6 and Ce/Fe-15/3) facilitates the phosphate adsorption of cerium carbonate active components. According to the SEM images, we find that the amorphous granular structure (with high Fe content) and the chunky structure (with low Fe content) both show decreased adsorption capacity for phosphate. The four adsorbents (Ce/Fe-12/6 to Ce/Fe-15/3) with Ce:Fe ratios of 12:6, 13:5, 14:4, and 15:3 exhibit flake morphology and demonstrate the best adsorption performance.

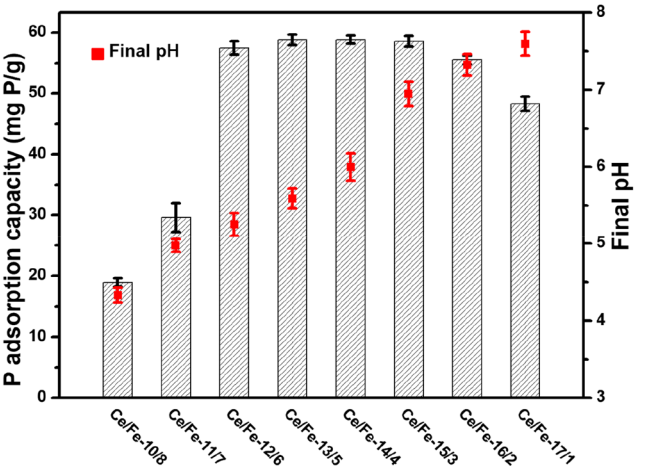

Figure 4. Static phosphate adsorption capacity and final pH of different ratios of Ce/Fe adsorbents (25 °C, reaction time = 48 h, C_0 = 30 mg P/L, adsorbent dosage = 0.5 g/L).

On the other aspect, the effluent pH of these eight samples increases from 4.3 to 7.6 with the decreasing Fe content. Because natural water bodies often have pH ranging from 6 to 9, Ce/Fe-15/3 with high adsorption capacity and near neutral effluent pH appears to be suitable for applications.

3.3. Effect of Competing Anions on the Phosphate Removal of Different Adsorbents. To investigate the selectivity of these adsorbents toward phosphate adsorption, we introduce various naturally occurring anions, including Cl^-, SO_4^{2-}, NO_3^-, HCO_3^-, SiO_3^{2-}, and HA, to the phosphate solution and conduct the static adsorption experiments on four adsorbents (pure $Ce_2(CO_3)_3{\cdot}xH_2O$, Ce/Fe-10/8, Ce/Fe-15/3, and Ce/Fe-17/1) for 48 h. The concentration of each competing anion is set to several times the phosphate concentration (from 0 to 20 in the molar ratio). The effect of competing ions on the P adsorption capacity of the four adsorbents is shown in Figure 5a−d. Replications of the test are done on Ce/Fe-15/3 (Figure S3a) to demonstrate the excellent reproducibility. In general, Ce/Fe-10/8 showed the worst adsorption capacity in all solutions (Figure 5b), as expected, because of it high iron content. The other three adsorbents all exhibit stable adsorption capacities in the presence of Cl^-, SO_4^{2-}, and NO_3^- while showing decreased adsorption capacities when HCO_3^-, SiO_3^{2-}, or HA are presented. In particular, the effects of Cl^- and NO_3^- on the phosphorus removal of Ce/Fe-15/3 are very weak, and the

https://doi.org/10.1021/acsomega.2c02269
ACS Omega 2022, 7, 31767−31777

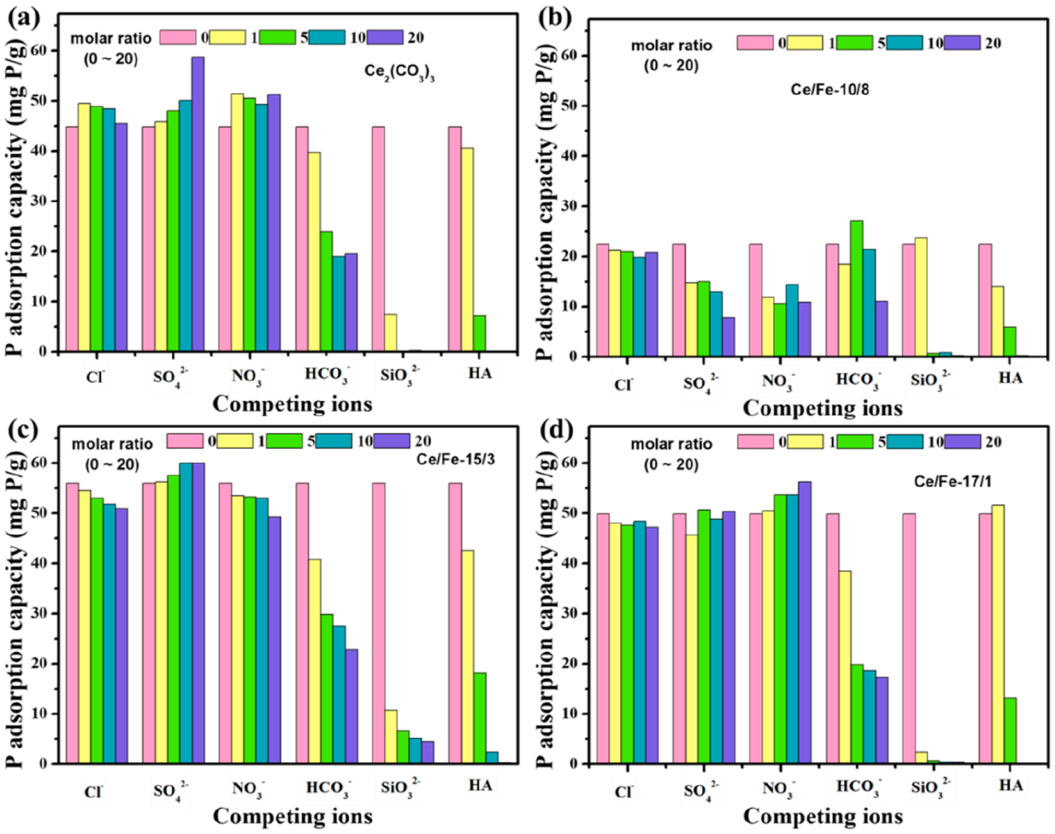

Figure 5. Effect of coexisting ions on the P adsorption capacity of (a) $Ce_2(CO_3)_3$, (b) Ce/Fe-10/8, (c) Ce/Fe-15/3, and (d) Ce/Fe-17/1 (25 °C, reaction time = 48 h, C_0 = 30 mg P/L, adsorbent dosage = 0.5 g/L, the concentration of competing ions was displayed as the molar ratio to phosphate).

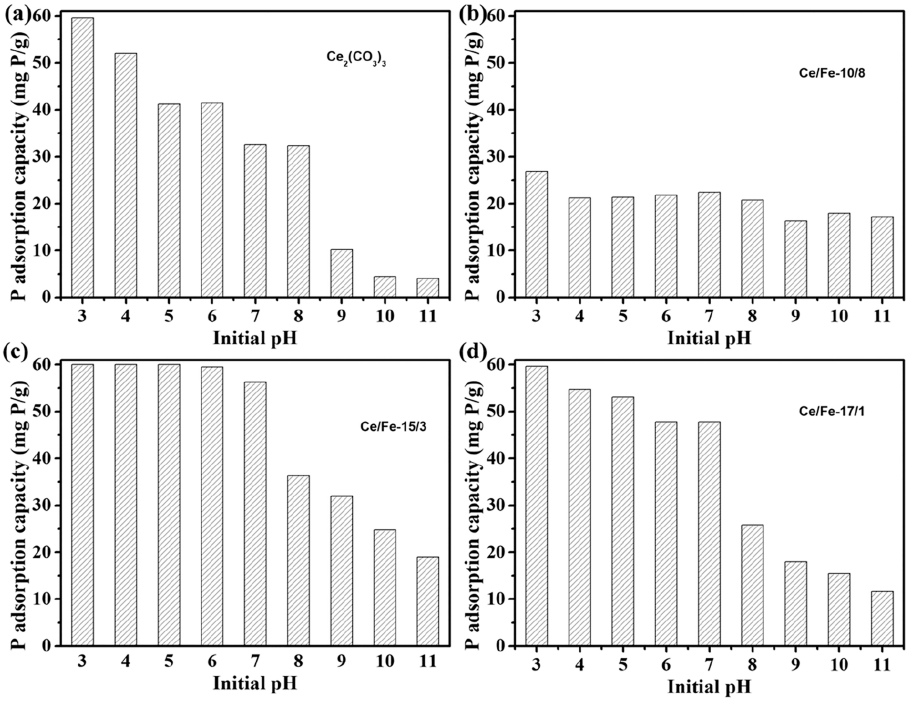

Figure 6. Effect of solution pH on the P adsorption capacity of (a) pure $Ce_2(CO_3)_3{\cdot}xH_2O$, (b) Ce/Fe-10/8, (c) Ce/Fe-15/3, and (d) Ce/Fe-17/1 (25 °C, reaction time = 48 h, C_0 = 30 mg P/L, adsorbent dosage = 0.5 g/L).

adsorption capacity maintains more than 50 mg P/g (even when the competing ion concentration is 20 times the phosphate concentration). The presence of SO_4^{2-} even slightly promotes the phosphorus adsorption on Ce/Fe-15/3. In

https://doi.org/10.1021/acsomega.2c02269
ACS Omega 2022, 7, 31767−31777

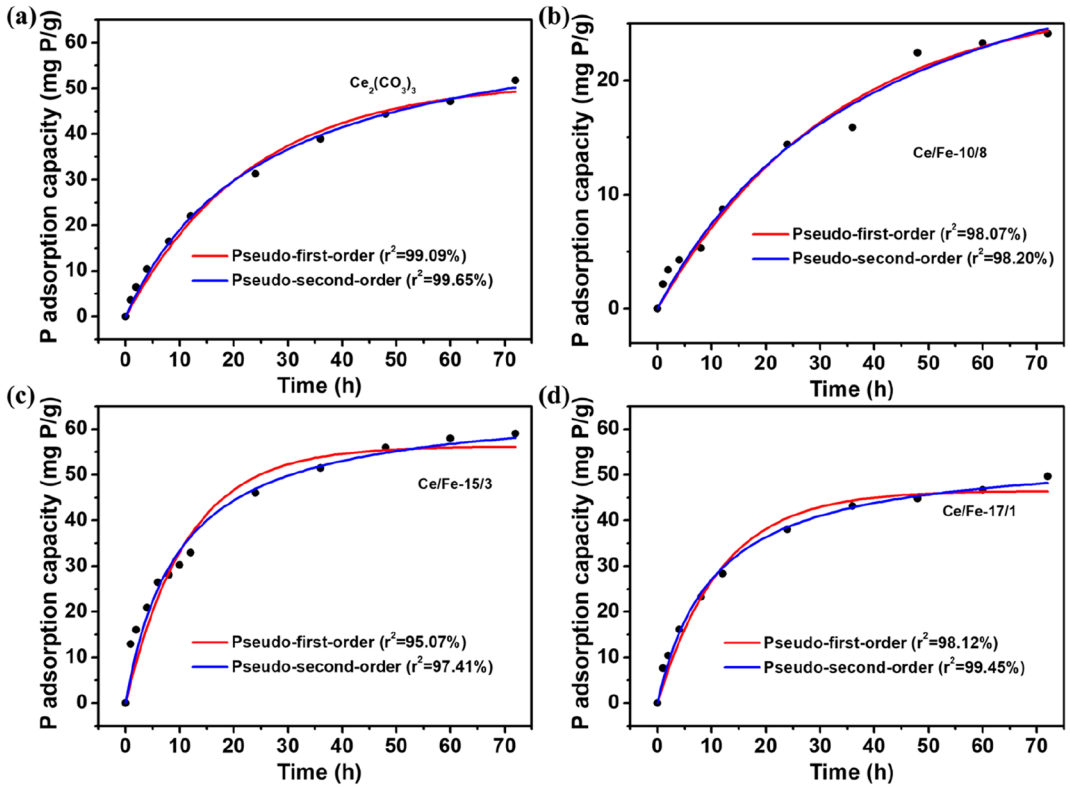

Figure 7. Adsorption kinetic data and the fitting curves of (a) $Ce_2(CO_3)_3$, (b) Ce/Fe-10/8, (c) Ce/Fe-15/3, and (d) Ce/Fe-17/1 (25 °C, C_0 = 30 mg P/L, adsorbent dosage = 0.5 g/L).

contrast, HCO_3^-, SiO_3^{2-}, and humic acid ions significantly decrease the phosphate adsorption capacity. When the molar ratio between HCO_3^- and the phosphate ions reaches 20:1, the adsorption capacity decreases to only 20 mg P/g. The effects of SiO_3^{2-} and humic acid ions are more severe, especially at high concentrations. However, it is worth noting that although the presence of HCO_3^-, SiO_3^{2-}, and humic acid ions affects the phosphate adsorption capacity of Ce/Fe-15/3 (Figure 5c), the negative impact is the least among all of the tested adsorbents.

3.4. Effect of Solution pH on the Phosphate Removal of Different Adsorbents. Because the pH value of the phosphorus-containing solution usually affects the adsorption process, we set the pH range to 3−11 for exploring its influence on the phosphate adsorption of four adsorbents (pure $Ce_2(CO_3)_3{\cdot}xH_2O$, Ce/Fe-10/8, Ce/Fe-15/3, and Ce/Fe-17/1). The adsorption period is set to 48 h, and the adsorption capacity values are shown in Figure 6a−d. Replications of the test are done on Ce/Fe-15/3 (Figure S3b) to demonstrate the excellent reproducibility. For pure $Ce_2(CO_3)_3{\cdot}xH_2O$, the adsorption capacity is the highest when the solution pH equals 3, and the adsorption capacity decreases gradually with the increasing solution pH. For Ce/Fe-10/8, the adsorption capacity remains relatively low (<30 mg P/g) but stable across the tested pH range. For Ce/Fe-15/3, in acidic environments (pH = 3−7), the 48 h adsorption capacity maintains an outstanding level of more than 55 mg P/g. Meanwhile, it is clear that the adsorption capacity decreases slightly from 60.00 mg P/g (pH = 3) to 56.21 mg P/g (pH = 7) with the increasing pH, indicating that the adsorption kinetics may be affected by solution pH. Indeed, in the alkaline region (8−11), the adsorption capacity further decreases to 36.48, 31.98, 24.72, and 19.15 mg P/g for pHs of 8, 9, 10, and 11, respectively. Finally, Ce/Fe-17/1 exhibits similar behavior as Ce/Fe-15/3 but with lower adsorption capacity because of the low iron doping level.

It is clear that for the adsorbents with cerium carbonate as the major component, the adsorption capacity is maintained at higher levels in acidic environments and decreases in basic conditions. Protons likely facilitate the dissolution of cerium carbonate and therefore increase the exchange between carbonate ions and phosphate ions. With the increasing amorphousness in the structure (in the order of $Ce_2(CO_3)_3{\cdot}xH_2O$, Ce/Fe-17/1, Ce/Fe-15/3, Ce/Fe-10/8), the pH stability increases. The iron doping introduces active sites on the cerium carbonate component and helps improve its adsorption in basic conditions. However, with the high iron content, the amorphous adsorbents exhibit limited adsorption capacity even in the low-pH region, which supports the necessity of having cerium carbonate for high capacity.

Meanwhile, another important consideration for investigating the pH stability is the effluent pH, which could lead to secondary pollution. For Ce/Fe-15/3, the change in final pH is consistent with the initial pH (Figure S4). When the influent pH is between 4 and 9, the effluent pH values are in the range of 6.5−8.5, which is ideal for discharging. For Ce/Fe-15/3, we took 20 mL of the postadsorption solution (with an initial pH of 3) to determine the Fe dissolution in the acidic condition. The ICP results show that the Fe leaching is only 10.025 μg/L, which confirms the negligible dissolution during the adsorption process.

3.5. Phosphate Adsorption Kinetics. To probe the adsorption process, we investigate the phosphate adsorption kinetics of different adsorbents in the 30 mg P/L phosphorus-

https://doi.org/10.1021/acsomega.2c02269
ACS Omega 2022, 7, 31767−31777

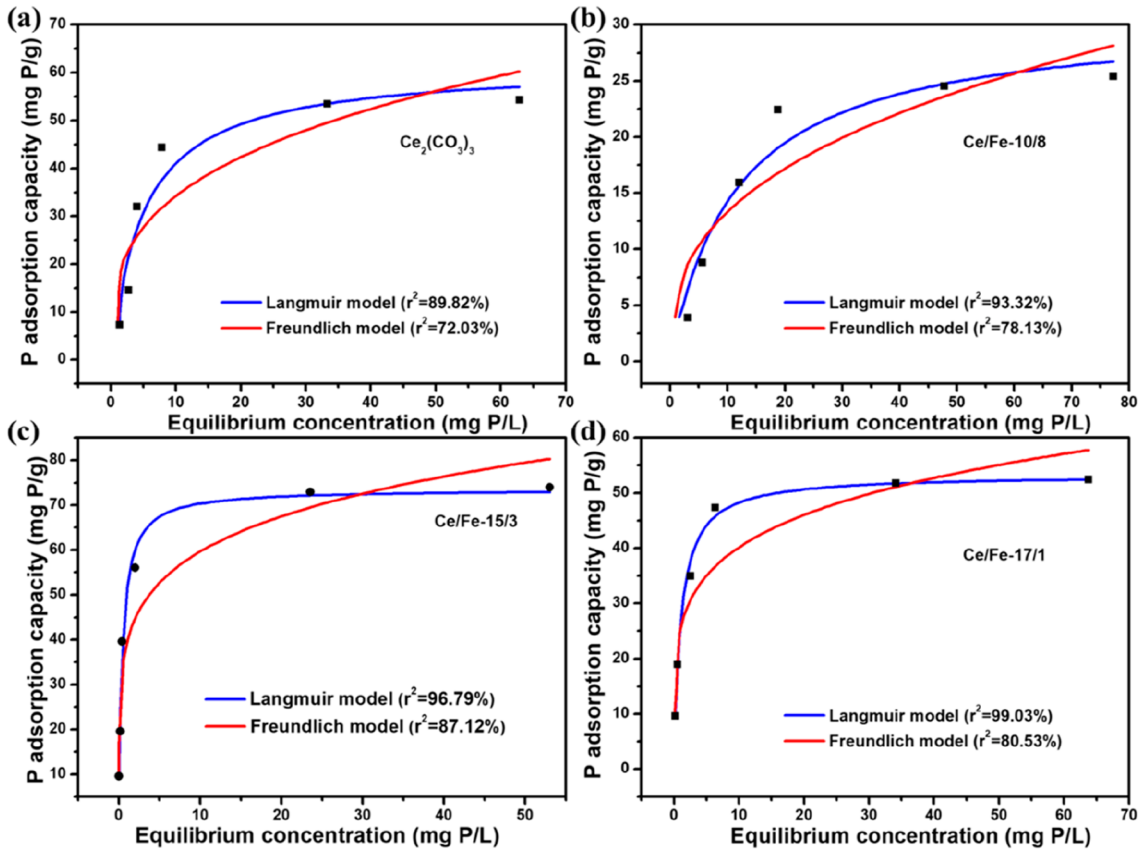

Figure 8. Adsorption isotherms of (a) pure $Ce_2(CO_3)_3{\cdot}xH_2O$, (b) Ce/Fe-10/8, (c) Ce/Fe-15/3, and (d) Ce/Fe-17/1 (25 °C, reaction time = 48 h, pH = 7, adsorbent dosage = 0.5 g/L).

containing solution. Replications of the test are done on Ce/Fe-15/3 (Figure S3c) to demonstrate the excellent reproducibility. Pseudo-first-order (PFO), pseudo-second-order (PSO), and Weber-Morris models are used to interpret the adsorption kinetics of four adsorbents (pure $Ce_2(CO_3)_3{\cdot}xH_2O$, Ce/Fe-10/8, Ce/Fe-15/3, and Ce/Fe-17/1), and the results are shown in Tables S1−S5 as well as Figures 7 and S5. According to the r^2 values, the pseudo-second-order kinetic model has a better fit for the adsorption process of all four adsorbents. The adsorption capacities of $Ce_2(CO_3)_3$ and Ce/Fe-17/1 are both near 50 mg P/g after 72 h. Ce/Fe-15/3 also exhibits adsorption capacity up to 60 mg P/g. However, Ce/Fe-10/8 with the highest Fe content shows adsorption capacity of only 25 mg P/g. According to the definition of the pseudo-second-order kinetic model, the adsorption rate on phosphate is mainly controlled by the active sites on the surface, and the adsorption rate increases with the increase of the number of active sites on the surface, indicating that the adsorption rate is controlled by the second-order rate equation.[30]

3.6. Phosphate Adsorption Isotherms. To further understand the adsorption behavior of the adsorbents, adsorption isotherms are measured to determine the maximum adsorption capacity at different phosphate concentrations (5−90 mg P/L, pH = 7) at 25 °C. Replications of the test are done on Ce/Fe-15/3 (Figure S3d) to demonstrate the reproducibility. We use different models (e.g., Langmuir, Freundlich, and Temkin models) to fit the isotherms, and the resulting parameters from the fitting processes are summarized in Tables S6−S10 as well as Figures 8 and S6. Based on the r^2 values, the Langmuir model provides the best fitting results for the adsorption isotherms of all four adsorbents. The maximum adsorption capacities of pure $Ce_2(CO_3)_3{\cdot}xH_2O$ and Ce/Fe-17/1 are both near 50 mg P/g, while that of Ce/Fe-10/8 is only 25 mg P/g. It is clear that Ce/Fe-15/3 has the best phosphate adsorption properties. When the initial phosphorus concentration is less than 30 mg P/L, Ce/Fe-15/3 adsorbs nearly all of the phosphate ions in the solution. The maximum adsorption capacity of Ce/Fe-15/3 reaches 73.98 mg P/g when the initial phosphorus concentration is 90 mg P/L. According to the definition of the Langmuir model, the adsorption process of phosphorus on Ce/Fe-15/3 should be monolayer adsorption, indicating that the active adsorption sites on the surface of Ce/Fe-15/3 have homogeneous distribution, leading to the uniform monolayer adsorption.[31]

3.7. Adsorption Mechanism. To explore the adsorption mechanism, we characterize valence states of Fe and Ce in Ce/Fe-15/3 by XPS measurements. Figure 9a shows the wide-range XPS spectra of Ce/Fe-15/3 before and after the phosphate adsorption. The P 2p signal of the sample after the adsorption (Ce/Fe-15/3) can be clearly observed on the spectrum. In the high-resolution P spectrum (Figure 9b), we find that the P 2p binding energy is ∼133.3 eV, different from the P 2p signal of KH_2PO_4 (134.0 eV).[32] Considering the absence of the P 2p signal on Ce/Fe-15/3, it is clear that new bonds are created by phosphate adsorption. This bonding is likely attributed to the chemical interaction between phosphate ions and Ce/Fe.

In the Fe 2p spectrum of Ce/Fe-15/3 (Figure 9c), the characteristic Fe(III) $2p_{1/2}$ signal is located at 724.8 eV, and the characteristic Fe(III) $2p_{3/2}$ signal is observed at 711.2 eV.[33]

https://doi.org/10.1021/acsomega.2c02269
ACS Omega 2022, 7, 31767−31777

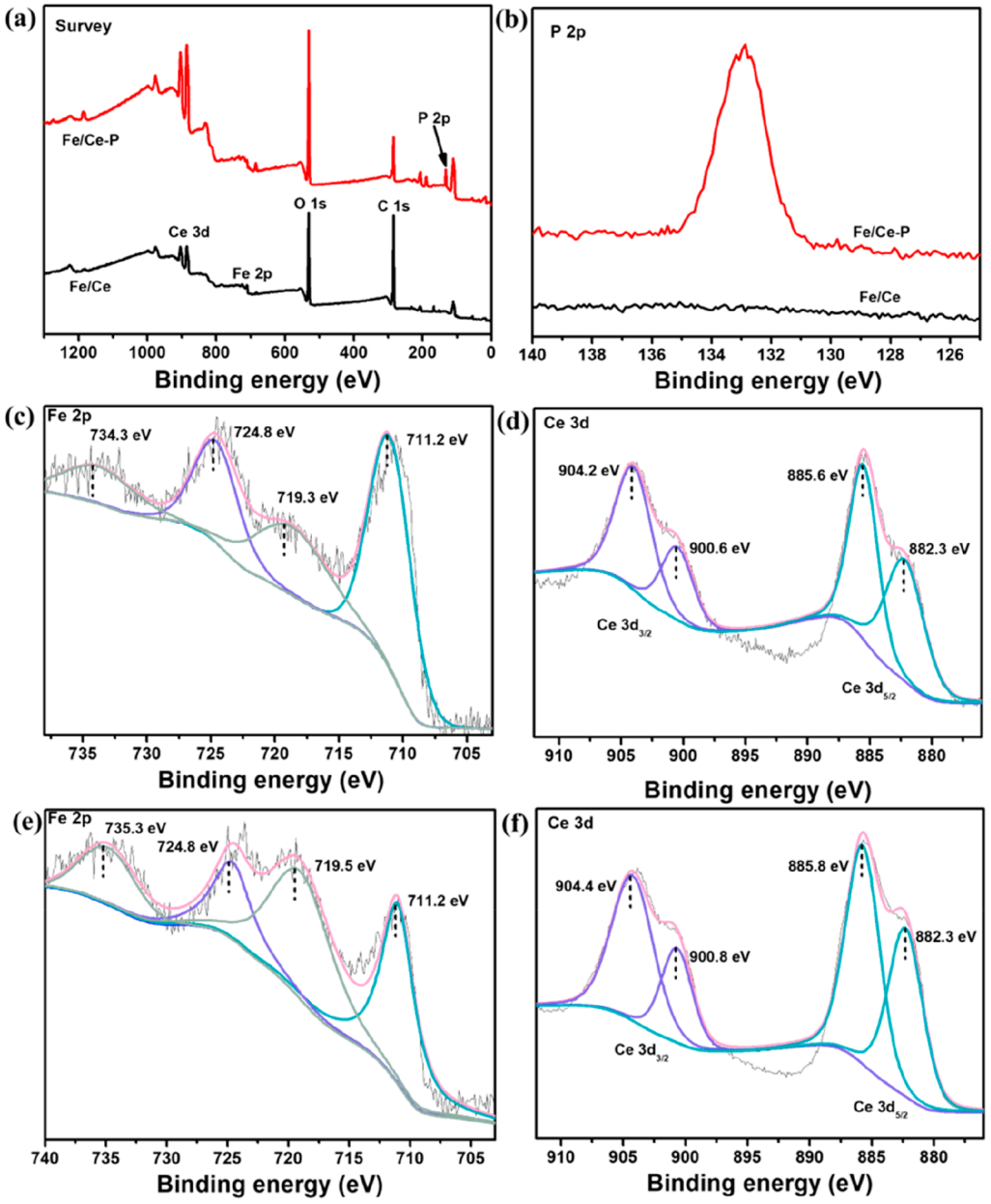

Figure 9. XPS scan spectra of Ce/Fe-15/3: (a) survey scan; (b) P 2p high-resolution spectrum; Fe 2p and Ce 3d high-resolution spectra before (c,d) and after (e,f) the P adsorption.

The two signals obtained at 734.3 and 719.3 eV are considered as satellite peaks. As for the Ce 3d spectrum of Ce/Fe-15/3 (Figure 9d), the characteristic Ce $3d_{5/2}$ signals are located at 882.3 and 885.6 eV, while the Ce $3d_{3/2}$ signals are observed at 900.6 and 904.2 eV. These signals are all attributed to the presence of Ce(III).[34]

After the adsorption process, we can see that the peak positions remain similar on the Fe 2p and Ce 3d spectra, indicating that both Fe(III) and Ce(III) maintain their oxidation states during the adsorption. The two major peaks on the Fe(III) spectrum are at 724.8 and 711.2 eV in Figure 9e, with two satellite peaks at 719.5 and 735.3 eV. Compared with the sample before adsorption, the binding energies of the two major peaks do not change, but the two satellite peaks move to slightly higher binding energy and exhibit increased intensity. These changes reveal the formation of new chemical environment for Fe(III) during the phosphate adsorption. Meanwhile, in Figure 9f, the two signals of Ce $3d_{3/2}$ are at 904.4 and 900.8 eV, while those of Ce $3d_{5/2}$ are at 885.8 and 882.3 eV. These signals are similar to the high-resolution Ce 3d spectrum before phosphate adsorption except for a slight increase of 0.2 eV in the binding energy. This observation also confirms the chemical environment change of the Ce(III) species. Hence, the adsorption of phosphate on Ce/Fe-15/3 likely proceeds via chemisorption, which relies on the active Fe(III) and Ce(III) sites. The chemisorption process leads to the changing coordination environment, which is reflected on the Fe 2p and Ce 3d XPS spectra.

4. CONCLUSION

In summary, we have successfully synthesized a promising Ce/Fe absorbent, Ce/Fe-15/3, by optimizing the ratio of cerium

https://doi.org/10.1021/acsomega.2c02269
ACS Omega 2022, 7, 31767−31777

and iron to Ce:Fe = 5:1. The adsorbent effectively removes phosphate ions from aqueous solutions. The differences in the crystal structure, morphology, and adsorption behaviors caused by different Ce/Fe ratios are characterized and analyzed. By conducting comprehensive analysis with XRD, FTIR, and SEM, we find that the amorphous granular structure and large chunky structure created by the high and low Fe content, respectively, both had a negative effect in the adsorption capacity of phosphate. With the optimized iron content, Ce/Fe-15/3 exhibits a high adsorption capacity of 58 mg P/g while demonstrating excellent selectivity toward phosphate adsorption in Cl^-, SO_4^{2-}, and NO_3^- solutions. The adsorption mechanism is characterized by XPS measurements, which indicate that the phosphate adsorption by Ce/Fe-15/3 is a combination effect of Ce/PO_4^{3-} and Fe/PO_4^{3-} chemical interactions. The simple bimetal modification strategy may provide a straightforward method for improving the adsorption properties of other rare-earth carbonate adsorbents.

■ ASSOCIATED CONTENT

Supporting Information

The Supporting Information is available free of charge at https://pubs.acs.org/doi/10.1021/acsomega.2c02269.

Supporting tables and figures are available in the Supporting Information: The elemental composition of Ce/Fe compounds; the adsorption kinetic fitting results of different Ce/Fe compounds; TGA characterization of selected Ce/Fe compounds (PDF)

■ AUTHOR INFORMATION

Corresponding Authors

Wei Wang − *CAS Key Laboratory of Design and Assembly of Functional Nanostructures, and Fujian Provincial Key Laboratory of Nanomaterials, Fujian Institute of Research on the Structure of Matter, Chinese Academy of Sciences, Fuzhou 350002, China; Xiamen Institute of Rare Earth Materials, Haixi Institute, Chinese Academy of Sciences, Xiamen 361021, China;* orcid.org/0000-0003-3178-236X; Email: wangwei@fjirsm.ac.cn

Xin Ye − *Key Laboratory of Urban Pollutant Conversion, Institute of Urban Environment, Chinese Academy of Sciences, Xiamen 361021, China;* orcid.org/0000-0003-2277-5328; Email: xye@iue.ac.cn

Authors

Jie Yang − *CAS Key Laboratory of Design and Assembly of Functional Nanostructures, and Fujian Provincial Key Laboratory of Nanomaterials, Fujian Institute of Research on the Structure of Matter, Chinese Academy of Sciences, Fuzhou 350002, China; Xiamen Institute of Rare Earth Materials, Haixi Institute, Chinese Academy of Sciences, Xiamen 361021, China*

Zuobei Wang − *CAS Key Laboratory of Design and Assembly of Functional Nanostructures, and Fujian Provincial Key Laboratory of Nanomaterials, Fujian Institute of Research on the Structure of Matter, Chinese Academy of Sciences, Fuzhou 350002, China; Xiamen Institute of Rare Earth Materials, Haixi Institute, Chinese Academy of Sciences, Xiamen 361021, China*

Ruonan Li − *CAS Key Laboratory of Design and Assembly of Functional Nanostructures, and Fujian Provincial Key Laboratory of Nanomaterials, Fujian Institute of Research on the Structure of Matter, Chinese Academy of Sciences, Fuzhou 350002, China; Xiamen Institute of Rare Earth Materials, Haixi Institute, Chinese Academy of Sciences, Xiamen 361021, China*

Xiaofeng Xu − *CAS Key Laboratory of Design and Assembly of Functional Nanostructures, and Fujian Provincial Key Laboratory of Nanomaterials, Fujian Institute of Research on the Structure of Matter, Chinese Academy of Sciences, Fuzhou 350002, China; Xiamen Institute of Rare Earth Materials, Haixi Institute, Chinese Academy of Sciences, Xiamen 361021, China*

Junrui Liu − *CAS Key Laboratory of Design and Assembly of Functional Nanostructures, and Fujian Provincial Key Laboratory of Nanomaterials, Fujian Institute of Research on the Structure of Matter, Chinese Academy of Sciences, Fuzhou 350002, China; Xiamen Institute of Rare Earth Materials, Haixi Institute, Chinese Academy of Sciences, Xiamen 361021, China*

You-Gui Huang − *CAS Key Laboratory of Design and Assembly of Functional Nanostructures, and Fujian Provincial Key Laboratory of Nanomaterials, Fujian Institute of Research on the Structure of Matter, Chinese Academy of Sciences, Fuzhou 350002, China; Xiamen Institute of Rare Earth Materials, Haixi Institute, Chinese Academy of Sciences, Xiamen 361021, China;* orcid.org/0000-0001-9962-3723

Complete contact information is available at: https://pubs.acs.org/10.1021/acsomega.2c02269

Notes

The authors declare no competing financial interest.

■ ACKNOWLEDGMENTS

We thank the financial support from the Youth Innovation Promotion Association CAS (No. 2021302 and No. 2021305) and the FJIRSM&IUE Joint Research Fund (No. RHZX-2019-003).

■ REFERENCES

(1) Yu, R.; Shi, Y.; Yang, D.; Liu, Y.; Qu, J.; Yu, Z.-Z. Graphene oxide/chitosan aerogel microspheres with honeycomb-cobweb and radially oriented microchannel structures for broad-spectrum and rapid adsorption of water contaminants. *ACS Appl. Mater. Interfaces* **2017**, *9*, 21809−21819.

(2) Morelli, B.; Hawkins, T. R.; Niblick, B.; Henderson, A. D.; Golden, H. E.; Compton, J. E.; Cooter, E. J.; Bare, J. C. Critical review of eutrophication models for life cycle assessment. *Environ. Sci. Technol.* **2018**, *52*, 9562−9578.

(3) Conley, D. J.; Paerl, H. W.; Howarth, R. W.; Boesch, D. F.; Seitzinger, S. P.; et al. Controlling eutrophication: Nitrogen and phosphorus. *Science* **2009**, *323*, 1014−1015.

(4) Kaiserli, A.; Voutsa, D.; Samara, C. Phosphorus fractionation in lake sediments–lakes Volvi and Koronia, N. Greece. *Chemosphere* **2002**, *46*, 1147−1155.

(5) Altmann, J.; Sperlich, A.; Jekel, M. Integrating organic micropollutant removal into tertiary filtration: Combining PAC adsorption with advanced phosphorus removal. *Water Res.* **2015**, *84*, 58−65.

(6) Diao, J.; Shao, L.; Liu, D.; Qiao, Y.; Tan, W.; Wu, L.; Xie, B. Removal of phosphorus from leach liquor of steel slag: Adsorption dephosphorization with activated alumina. *Jom* **2018**, *70*, 2027−2032.

(7) Wang, Z.; Nie, E.; Li, J.; Yang, M.; Zhao, Y.; Luo, X.; Zheng, Z. Equilibrium and kinetics of adsorption of phosphate onto iron-doped activated carbon. *Environ. Sci. Pollut. Res. Int.* **2012**, *19*, 2908−17.

(8) Silva, M.; Baltrusaitis, J. A review of phosphate adsorption on Mg-containing materials: kinetics, equilibrium, and mechanistic insights. *Environ Sci Water Res Technol* **2020**, *6*, 3178−3194.
(9) Liu, Y.; Cao, X. L.; Wang, W.; Li, G. L.; Li, S.; Huang, Y. G. A Linear Ce(III) Complex Based on in-situ Generated N-hydroxy-1,8-naphthalenedicarboximide. *Chinese J. Struc Chem.* **2021**, *40*, 1475−1481.
(10) Zhu, D.; Liang, J.; Ding, Y.; Xu, A. Application of far infrared rare earth mineral composite materials to liquefied petroleum gas. *J. Nanosci. Nanotechno.* **2010**, *10*, 1676−1680.
(11) Li, R.; Li, Q.; Gao, S.; Shang, J. K. Exceptional arsenic adsorption performance of hydrous cerium oxide nanoparticles: Part A. Adsorption capacity and mechanism. *Chem. Eng. J.* **2012**, *185*−*186*, 127−135.
(12) Na, C. K.; Park, H. J. Defluoridation from aqueous solution by lanthanum hydroxide. *J. Hazard. Mater.* **2010**, *183*, 512−20.
(13) Goscianska, J.; Ptaszkowska-Koniarz, M.; Frankowski, M.; Franus, M.; Panek, R.; Franus, W. Removal of phosphate from water by lanthanum-modified zeolites obtained from fly ash. *J. Colloid Interface Sci.* **2018**, *513*, 72−81.
(14) Lu, Y.; Wu, H.; Xia, Y.; Huang, M. Strong adsorption of phosphate by amorphous lanthanum carbonate nano-adsorbents. *Water Sci. Technol.* **2021**, *83*, 1605−1618.
(15) Liu, X.; Byrne, R. H. Rare earth and yttrium phosphate solubilities in aqueous solution. *Geochim. Cosmochim. Ac.* **1997**, *61*, 1625−1633.
(16) Firsching, F. H.; Brune, S. N. Solubility products of the trivalent rare-earth phosphates. *J. Chem. Eng. Data* **1991**, *36*, 93−95.
(17) Li, Y. Y.; Nirenberg, L. Estimates for elliptic systems from composite material. *Commun. Pur. Appl. Math.* **2003**, *56*, 892−925.
(18) Wu, Q.; You, R. R.; Wu, Q. P.; Chen, F. Y.; Yu, Y. Equilibrium and kinetics studies of phosphate removal from solution onto a hydrothermally modified Al-Si-Fe-Ca composite adsorbent. *Mater. Sci. Forum* **2014**, *787*, 128−134.
(19) Su, Y.; Yang, W.; Sun, W.; Li, Q.; Shang, J. K. Synthesis of mesoporous cerium−zirconium binary oxide nanoadsorbents by a solvothermal process and their effective adsorption of phosphate from water. *Chem. Eng. J.* **2015**, *268*, 270−279.
(20) Wang, L.; Wang, J.; He, C.; Lyu, W.; Zhang, W.; Yan, W.; Yang, L. Development of rare earth element doped magnetic biochars with enhanced phosphate adsorption performance. *Colloids Surf. A Physicochem. Eng. Asp.* **2019**, *561*, 236−243.
(21) Guo, H.; Li, W.; Wang, H.; Zhang, J.; Liu, Y.; Zhou, Y. A study of phosphate adsorption by different temperature treated hydrous cerium oxides. *Rare Metals* **2011**, *30*, 58−62.
(22) Wang, C.; Zhang, X.; Li, J.; Qi, X.; Guo, Z.; Wei, H.; Chu, H. Gold nanoparticles on nanosheets derived from layered rare-earth hydroxides for catalytic glycerol-to-lactic acid conversion. *ACS Appl. Mater. Interfaces* **2021**, *13*, 522−530.
(23) Lee, B.-I.; Lee, E.-s.; Byeon, S.-H. Assembly of layered rare-earth hydroxide nanosheets and SiO_2 nanoparticles to fabricate multifunctional transparent films capable of combinatorial color generation. *Adv. Funct. Mater.* **2012**, *22*, 3562−3569.
(24) Ali, A.; Andriyana, A. Properties of multifunctional composite materials based on nanomaterials: a review. *RSC Adv.* **2020**, *10*, 16390−16403.
(25) Skorulska, A.; Piszko, P.; Rybak, Z.; Szymonowicz, M.; Dobrzynski, M. Review on polymer, ceramic and composite materials for CAD/CAM indirect restorations in dentistry-application, mechanical characteristics and comparison. *Materials (Basel)* **2021**, *14*, 1592−1613.
(26) Park, S. H.; L Ee, C. E. Characterization of chain molecular assemblies in long-chain, lamellar copper alkylsulfonates: Self-assembled monolayer vs bilayer structure. *Chem. Mater.* **2006**, *18*, 981−987.
(27) Wakita, H.; Kinoshita, S. A synthetic study of the solid solutions in the systems $La_2(CO_3)_3 \cdot 8H_2O$-$Ce_2(CO_3)_3 \cdot 8H_2O$ and $La(OH)CO_3$-$Ce(OH)CO_3$. *Bull. Chem. Soc. Jpn.* **1979**, *52*, 428−432.
(28) Parikh, S. J.; Chorover, J. ATR-FTIR spectroscopy reveals bond formation during bacterial adhesion to iron oxide. *Langmuir* **2006**, *22*, 8492−8500.
(29) Salavati-Niasari, M.; Mir, N.; Davar, F. A novel precursor in preparation and characterization of nickel oxide nanoparticles via thermal decomposition approach. *J. Alloy. Compd.* **2010**, *493*, 163−168.
(30) Ho, Y. S.; Ofomaja, A. E. Pseudo-second-order model for lead ion sorption from aqueous solutions onto palm kernel fiber. *J. Hazard. Mater.* **2006**, *129*, 137−42.
(31) Jeppu, G. P.; Clement, T. P. A modified Langmuir-Freundlich isotherm model for simulating pH-dependent adsorption effects. *J. Contam. Hydrol.* **2012**, *129*−*130*, 46−53.
(32) Zhang, Q.; Teng, J.; Zou, G.; Peng, Q.; Du, Q.; Jiao, T.; Xiang, J. Efficient phosphate sequestration for water purification by unique sandwich-like mxene/magnetic iron oxide nanocomposites. *Nanoscale* **2016**, *8*, 7085−7093.
(33) Yamashita, T.; Hayes, P. Analysis of XPS spectra of Fe^{2+} and Fe^{3+} ions in oxide materials. *Appl. Surf. Sci.* **2008**, *254*, 2441−2449.
(34) Rygel, J. L.; Chen, Y.; Pantano, C. G.; Shibata, T.; Du, J.; Kokou, L.; Woodman, R.; Belcher, J. Local Structure of Cerium in Aluminophosphate and Silicophosphate Glasses. *J. Am. Ceram. Soc.* **2011**, *94*, 2442−2451.

https://doi.org/10.1021/acsomega.2c02269
ACS Omega 2022, 7, 31767−31777